ADVANCED FUNCTIONAL MATERIALS
www.afm-journal.de



# Hierarchical Superhydrophobic Surfaces Fabricated by Dual-Scale Electron-Beam-Lithography with Well-Ordered Secondary Nanostructures

*Jiansheng Feng, Mark T. Tuominen, and Jonathan P. Rothstein**

**Recent studies on superhydrophobic surfaces have revealed the important roles of structural hierarchy in the overall properties of these surfaces. Here, a novel, versatile, and efficient technique is introduced for fabricating macroscopic hierarchical superhydrophobic surfaces with both well-defined primary microstructures and well-ordered secondary nanostructures using electron-beam lithography. With this technique, the engineering capability of controlling the size, shape, and distribution of the secondary-features is demonstrated, which allows a systematic and quantitative study of the individual effects of these parameters. Superhydrophobic surfaces produced by this new technique exhibit two distinctive wetting behaviors, high and low adhesion. The structural characteristics and structure-property relations of each of those two regimes are discussed.**

## 1. Introduction

Hierarchical structures observed in nature have inspired scientific and engineering advances in fields such as hydrodynamics, surface physics, and materials science.[1–11] In resent literature, a broad range of interesting properties have been attributed to hierarchical surfaces including reversible adhesion,[6,12] controllable wettability,[4,13–15] and enhanced optoelectromagnetic activity.[16–18] One particular class of hierarchical surfaces, superhydrophobic surfaces, have received significant attention due to their self-cleaning and drag-reducing capabilities.[2,8–9,19–20] Superhydrophobic surfaces are surfaces with very high water contact-angles (CAs), typically greater than 150°. Previous studies based on artificial hierarchical superhydrophobic surfaces have revealed the importance of the secondary structures on the overall wetting properties of the surfaces. These secondary structures have been shown to enhance the contact angle (CA), reduce the CA-hysteresis, and improve the stability and robustness of superhydrophobic states.[2,8–11,15,19–28]

A number of methods have been reported for producing artificial hierarchical structures on a surface, including molding and imprinting,[5,14,16] chemical etching,[9,25,29] reactive-ion etching,[19,30] self-assembly,[21,31–34] deposition,[10,18,24] hydrothemal systhesis,[13] template guided gelation,[8] photolithography,[6,12] growth of nanowires,[23] electric-field-assisted soft lithography,[35] laser-assisted etching,[36] and ultrasonically assisted synthesis.[37] However, the majority of these hierarchical surfaces are decorated with random secondary structures, and thus only statistical conclusions can be drawn. These random secondary structures can sometimes vary significantly in size, orientation, and distribution, making it difficult to fully characterize the secondary structures and to correlate the details of these structures and the overall properties of hierarchical surfaces. In order to better understand the role of the secondary features, here, we introduce a novel technique for fabricating hierarchical surfaces with both well-defined primary structures and regular secondary structures by electron-beam lithography (EBL or e-beam lithography). Using this technique, multiple geometric parameters including size, spacing, and shape of both the primary and the secondary structures can be designed precisely and relatively independently. Moreover, we believe that the ability to fabricate macroscopic devices with well-defined hierarchical structures and at the same time maintain a very high level of control over the finest details of the structures will also be quite useful in many other important areas.

## 2. Dual-Scale Electron-Beam Lithography

Among current lithographic techniques, EBL offers one of the best combination of precision and versatility,[38,39] yet the utilization of EBL in fabricating macroscopic devices is often largely hindered by its limited throughput. This is the case when conventional e-Beam resists such as PMMA or polystyrene are used. However, this limitation can be significantly reduced if EBL is done on a more sensitive resist, such as SU-8 due to the drastic reduction of exposure dosage required.[40] SU-8 is well known as a high-performance photoresist for

J. Feng, Prof. M. T. Tuominen
Physics Department
University of Massachusetts
Amherst, United States
E-mail: jianshen@physics.umass.edu; tuominen@physics.umass.edu
Prof. J. P. Rothstein
Department of Mechanical and Industrial Engineering
University of Massachusetts
Amherst, United States
E-mail: rothstein@ecs.umass.edu

**DOI: 10.1002/adfm.201100665**

UV lithography, and is also very sensitive to electron-beam exposure.[40–42] From experiments we have found that, when SU-8 is used in EBL, the fabrication time per device is rather reasonable. For a typical 2 mm × 2 mm hierarchical surface, the total e-beam time which includes both time for electron beam exposure and stage movement is between 20 and 35 min.

Two types of hierarchical structures consisting of macroscopic arrays of well-defined micrometer-sized blocks and well-ordered nanometer-scale posts or ridges were fabricated on SU-8. The first type consisted of nanometer-scale posts covering only the top surfaces of the micrometer-sized blocks. The second type consisted of nanometer-scale posts or ridges covering both the top and the side surfaces of the micrometer-sized blocks, as well as the valleys between adjacent blocks. Correspondingly, two different fabrication techniques were investigated for imparting dual-scale structures to the desired surfaces: single and double EBL exposure.

### 2.1. Single Electron-Beam Lithography Exposure

In a single EBL-exposure process, a layer of SU-8 was first spin-coated onto a silicon wafer with a thickness between 10 μm and 15 μm using MicroChem SU-8 2010 or 2015 solutions. The photoresist then underwent a specially designed electron beam scan routine to write a dot pattern of sub-micrometer features. The center-to-center distance between nearby e-beam exposure locations was specified based on the desired spacing of the secondary features, while the post radius was controlled by the dosage of the e-beam. The proximity effect helped to simultaneously implement the primary features, specifically, elevated bases with a significantly larger length-scale (i.e., about 10 μm) were generated where the exposure density is high. A schematic diagram for single EBL exposure is shown in **Figure 1**a. Using this technique, the entire hierarchical structured surface was fabricated in one EBL step, and the secondary features only covered the tops of the micrometer-scale primary structures, as seen in **Figure 2**a. As a result, a very high level of control over the distributions of the secondary-features was possible. For example, Figure 2c demonstrates an array of primary blocks with alternating rough and smooth tops (i.e., with or without secondary features on top). On our scanning electron microscopy (SEM)–EBL system, the maximum field size an e-beam writing can cover without moving the stage is dictated by the magnification. This in turn affects the resolution of the lithography. To balance resolution

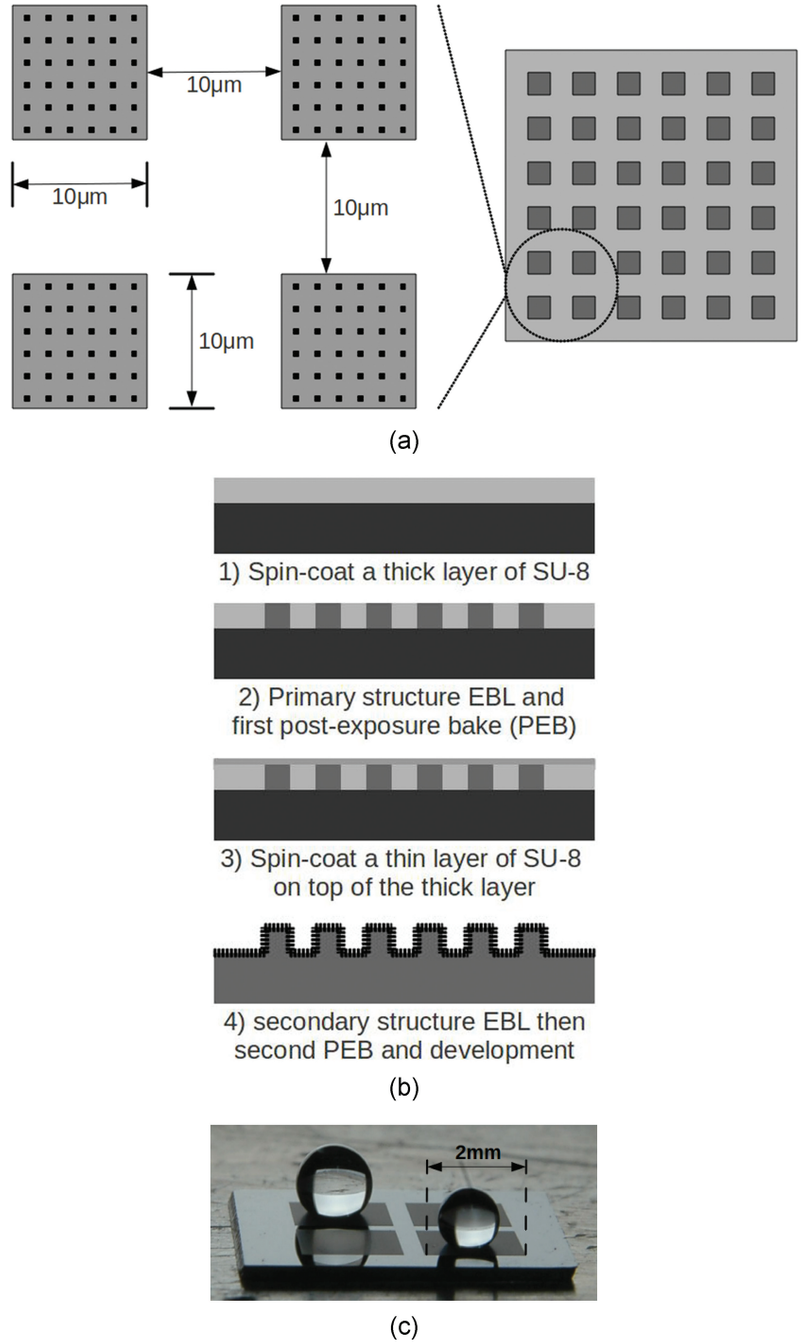


**Figure 1.** a) Schematic diagram of the hierarchical surfaces produced by a single EBL-exposure process. The secondary nanometer-features are directly written by e-beam lithography and the primary microstructures are generated by a proximity effect. This way, both the primary and the secondary structures are generated within a single step and the secondary features are only on the tops of the primary structrues. b) Schematic diagram of the fabrication of hierarchical SU-8 surfaces through a double EBL-exposure process. Each patch of the 2 × 2 array shown in (c) is a macroscopic superhydrophobic surface with 2 mm linear dimension.

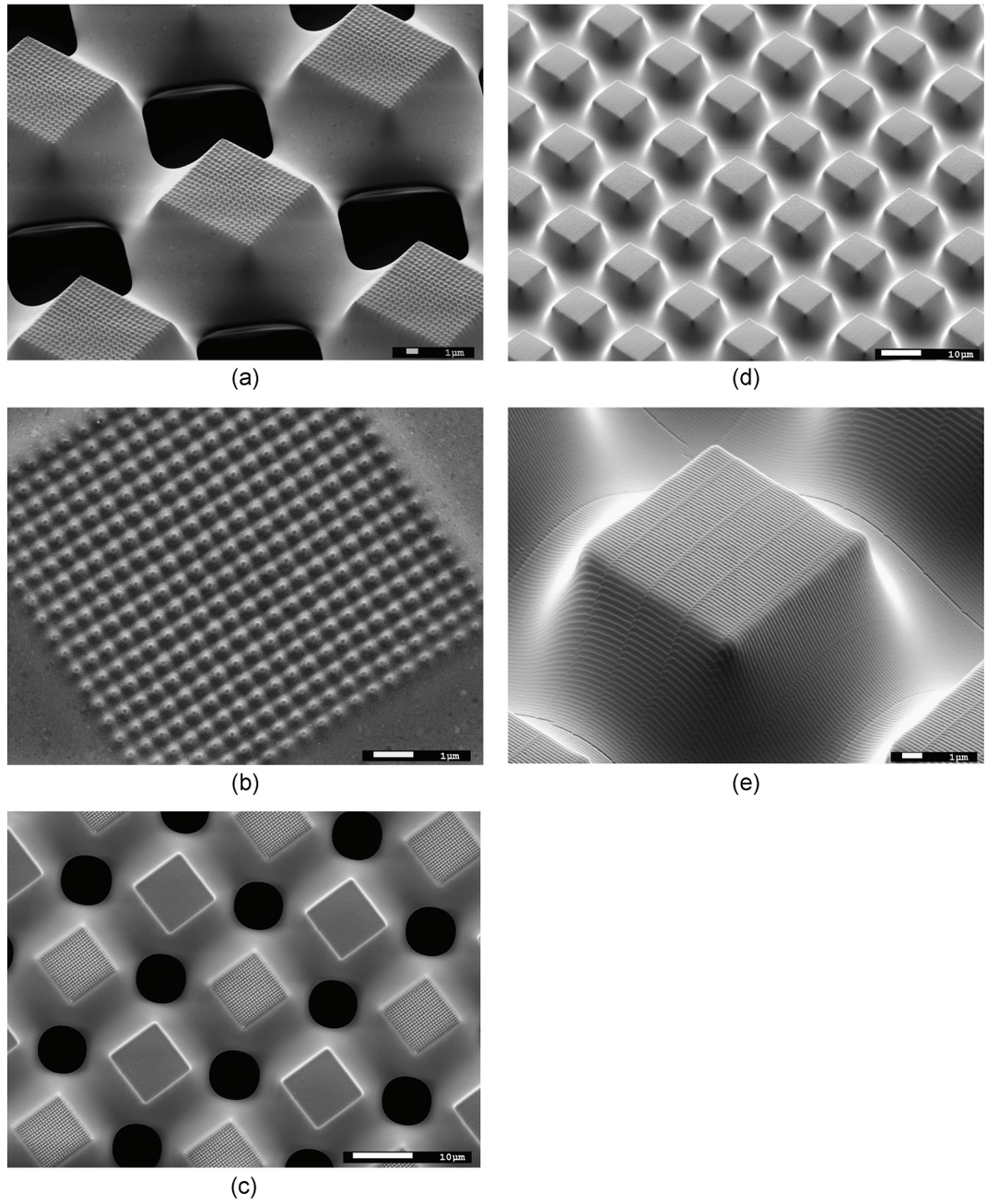


**Figure 2.** SEM images of hierarchical structures fabricated by dual-scale e-beam lithography. a,b) Single EBL exposure sample with secondary posts. The images are tilt by 45°-tilt (a) and viewed from the top (b). The secondary-feature shows a 500 nm period and aspect-ratio close to one. c) Single-exposure samples with althernating smooth and rough tops (top view). d,e) Double EBL-exposure sample with secondary ridges. Both images were taken at a 45° tilt. The primary blocks are of the dimension of about 10 µm × 10 µm × 8 µm. The secondary ridges show a 70 nm width and 200 nm period.

and efficiency, a magnification of 130×, which corresponds to a maximum writing field of 1 mm × 1 mm, was chosen and was found to provide acceptable writing resolution of both the micro- and nanometer-scale features. The total EBL time of a single-exposure sample (consists of four 2 mm × 2 mm surfaces) was between 15 and 45 min depending on the e-beam current used.

### 2.2. Double Electron-Beam Lithography Exposure

In order to fabricate hierarchical structures in which nanometer-features cover not only the tops of the micrometer features but also their sidewalls and the valleys between them, as seen in Figure 2d and e, we also experimented with a double-exposure procedure. The schematic of this procedure is

shown in Figure 1b. In a double-exposure process, a large-scale exposure, which can be achieved by either EBL or UV photolithography, was first performed on a thick layer (10 ≈ 15 μm) of SU-8 to induce cross-linking of the micrometer-scale primary features. In our experiments, we typically created an array of 10 μm × 10 μm square blocks, spaced 10 μm apart. After a post exposure bake (PEB-1), a thin layer of SU-8 on the order of 500 nm in thickness was spin-coated on top of the undeveloped layer. A second exposure with EBL was then applied to construct the secondary features over the entire surface. The best secondary structures were found to be written at a magnification of 650×, which corresponds to a field size of 200 μm × 200 μm. In this case, each 2 mm × 2 mm surface is covered by a 10 × 10 array of EBL patches. Lower magnifications can be used for lower resolution requirements and would require fewer patches. The surface was then put through a second post exposure bake (PEB-2) and finally it was developed, resulting in hierarchical structures, as shown in Figure 2e. For a double-exposure samples (consisting of four 2 mm × 2 mm surfaces), the first exposure took between 5 and 15 min, and the second exposure took between 30 min and 2 h depending on the magnification and beam current used.

### 2.3. Characterization of the Hierarchical Structures

SEM images of the hierarchical structures in Figure 2 illustrate the similarities and differences between the two prototypes of dual-scale EBL. The primary structures were designed in both cases to be 10 μm × 10 μm square blocks spaced 10 μm apart. Both 5 μm and 8 μm square blocks were also experimented as primary features and the resulting structures were similar. Swelling towards the base of the primary features and consequently the forming of bridges between nearby blocks is beneficial for enhancing adhesion between the structures and the substrate. Both ridges and posts have been implemented as the secondary-features with periods ranging from 200 nm to 500 nm. The secondary-features shown in Figure 2e are ridges with a width of 70 nm on average (at half height) and a height of 70 nm. These ridges cover the entire surface including the bottom of the valleys between the large posts. The spacing of the secondary ridges on some side surfaces (whose normal is roughly perpendicular to the direction of the ridges) have been increased due to the slope of the sidewall. These features were made possible by the large penetration depth and large depth of focus of the high-energy e-beam. In comparison, nanoposts, shown in Figure 2a, cover only the top of the primary features. The average diameter of these posts is around 200 nm with a designed period of 500 nm and average height of about 150 nm. Whether ridges or posts were produced in the second exposure was found to mainly depend on the beam current used with increasing current favoring ridges. In our SEM–EBL system, exposure carried out at 30 kV with a Probe Current (PC) 7 (corresponding to about 120 pA) or lower produced posts; exposure done with PC 8 (corresponding to about 220 pA) or higher produced ridges. Additionally, for both secondary ridges and posts, the feature size and height mainly depended on the exposure dosage and were found to be relatively insensitive to the thickness of the SU-8 layer. Among all our samples, the highest secondary-feature aspect-ratio was about 0.85 for ridges and 0.75 for posts. As always, the proficiency of the operator in beam alignment and aberration minization, and the capability to align the position of the second writing with the first one is critical to obtain high-quality reproducible lithography results.

## 3. Surface Wettability

A series of double-exposure hierarchical surfaces with identical primary (10 μm square posts spaced 10 μm apart) but variable secondary-features were fabricated for a comparative wettability study. After EBL, a 10 nm layer of silicon monoxide was thermally deposited on each sample surfaces and subsequently modified with a fluoroalkylsilane via a vapor-phase reaction (for more detail, see the Experimental Section). The surface properties were characterized with quasi-static measurements of the advancing and receding CAs. When measuring the CAs, care was taken to ensure the measurements represent the thermodynamic equilibrium states. A droplet of water with a diameter of approximately 1 mm was deposited on the hierarchical surfaces from a needle mounted approximately 0.5 mm above the surface. A syringe was then used to expand and contract the drop in order to measure the advancing and receding angles respectively. The measurements were taken from images captured with a video camera employing a long-distance-microscopy objective. An example of the resulting images can be found in **Figure 3**. These images were processed using ImageJ[43] to determine the CAs. Several cycles of the water droplet expansion and contraction were performed before each measurement to ensure that thermally stable CA values were measured. When conducting CA measurements on samples with secondary ridges, no attention was paid to the direction of the ridges with respect to the camera angle. Two distinctive behaviors were observed as the result of varying the secondary structures. First, a number of surfaces demonstrated high advancing CAs with low hysteresis. These low-adhesion surfaces are examples of what is known as the lotus effect, where the water remains in the Cassie state over both the micrometer-scale and nanometer-scale features on the surface. Second, high advancing CAs with high hysteresis were observed in some cases. These high-adhesion surfaces are examples of the rose-petal effect, where the water remains in the Cassie state over the large scale features, but fully wets and therefore exists in the Wenzel state on the nanometer-scale features, superimposed on the tops of the micrometer-scale posts. In some cases, with the secondary structures being either posts or ridges, pinning of contact line were clearly observed in the videos taken for CA measurements. In those cases, the CAs were determined based on the macroscopic profiles instead of the microscopic pined edges. Both high-adhesion and low-adhesion behavior were observed on double-exposure samples with secondary posts with periods of 200, 300, or 500 nm. Conversely, all of the double-exposure samples with secondary-ridges and all of the single-exposure samples showed high adhesion behavior regardless of the period of the secondary features.

An advancing and a receding water CA measured on each of our silanized double-exposure surfaces, together with their average values, are plotted on **Figure 4**a with error-bars to show

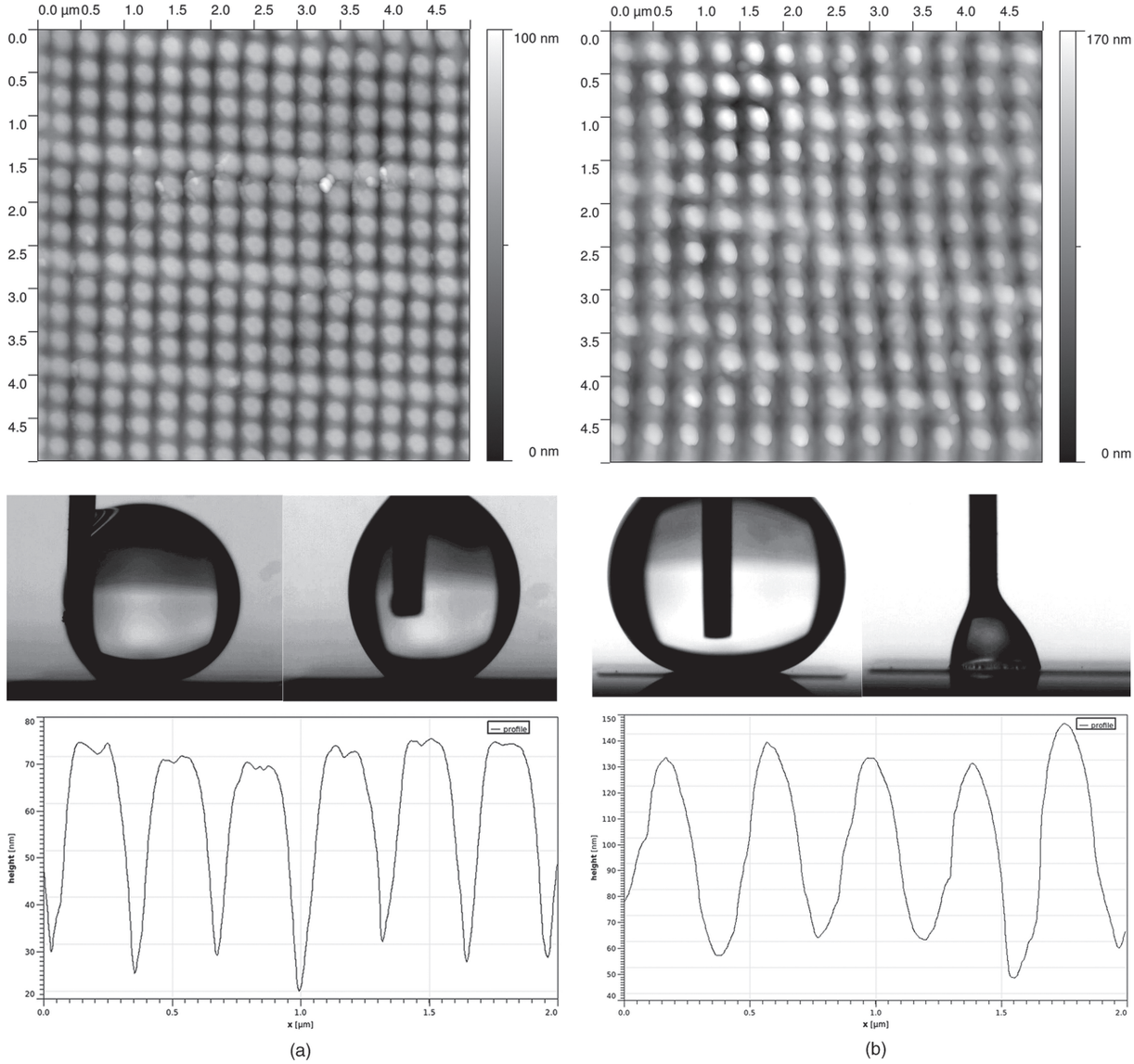


**Figure 3.** CA measurements and atomic force microscopy (AFM) images of the secondary structures. a) Example of low-adhesion surfaces. b) Example of high-adhesion surfaces.

the uncertainty. The advancing CAs for all the surfaces independent of secondary-feature spacings or geometries were found to remain fixed at 160° with variations of less than 5°. Therefore, all these hierarchical surfaces are superhydrophobic. This observation also suggests that the advancing CA is mainly set by the micrometer-scale features which, for these experiments, were fixed and not varied. The effect of varying secondary features on advancing CA is minimal. The receding CA values, on the other hand, appear to divide the data into the two regimes we have discussed earlier. In the low-adhesion cases, the receding CAs were found to reside above 120°. In the high-adhesion cases, the receding CAs were consistently below 90°, resulting in very large CA-hysteresis values. Unlike the advancing CA, the receding CA is found to depend on both the period and geometry of the secondary features. This can be quantified by performing linear regressions through the experimental data. As shown in Figure 4a, the advancing CAs appear to be statistically independent of secondary-feature period, varying by less than 1° for every 100 nm change in the period of the secondary feature. A statistically significant correlation was found between the secondary-feature period and the receding CA. This is most apparent for the high-adhesion cases where the receding CA was found to increase by more than 3° for every 100 nm increase in secondary-feature spacing. In the low-adhesion cases, the dependence was found to be significantly weaker.

Figure 4b compares the advancing and receding CAs measured on various structured surfaces. With the same surface-chemistry treatment, the average advancing CAs of all

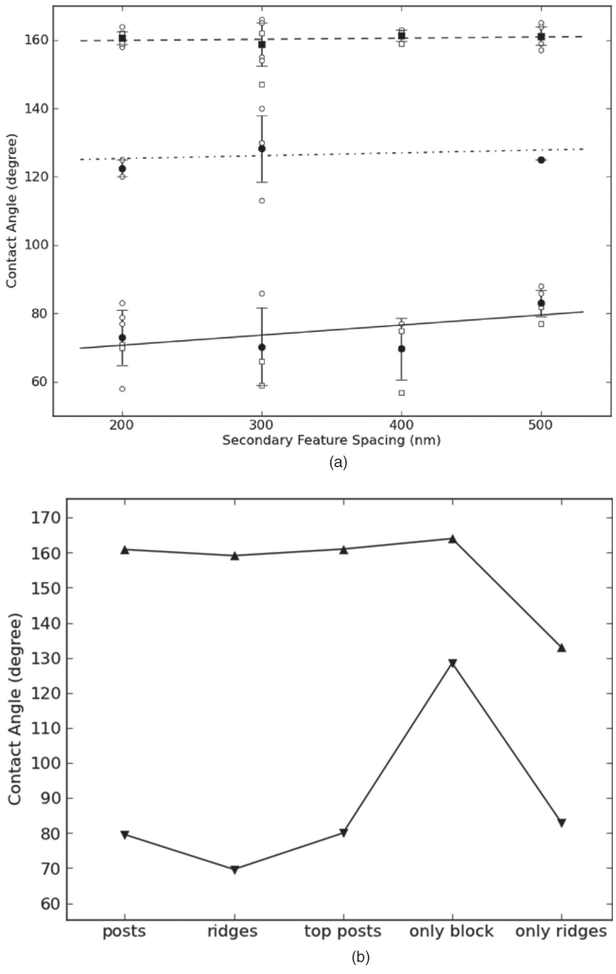


**Figure 4.** Advancing and receding CAs of water droplets on silanized hierarchical surfaces. a) Samples with secondary-features covering the entire surface. Raw data-points are represented by open symbles. Open circles correspond to samples with secondary-posts and open squares correspond to samples with secondary-ridges. Notice some raw-data-point overlap. Average values are represented by closed symbols (with error bars). Solid squares correspond to average advancing CAs, and solid circles correspond to average receding Cas. Also shown are linear fits for advancing CAs (dashed line), receding CA of low-adhesion cases (dash-dotted line), and receding CA of high-adhesion cases (solid line). b) Average advancing (▲) and receding (▼) contact angles of various structrued surfaces: 1) hierarchical surface with secondary post all over; 2) hierarchical surface with secondary ridges all over; 3) hierarchical surface with secondary posts on the tops only; 4) surface with only 10-μm blocks; 5) surface with nanoridges only.

hierarchical surfaces in our experiments were the same as that of a surface with only 10 μm blocks but about 30° greater than that of a surface with only nanoridges (300 nm period). This is additional evidence that the advancing CA is dictated primarily by the primary features. The average receding CAs of the hierarchical surfaces in the high-adhesion zone were close to that of the nanoridges-decorated surface and about 50° lower than that of the surface with only micrometer blocks. These observations indicate that, for a hierarchical surface, the advancing CA is mainly determined by the primary structures and the receding CA by the secondary structures, which is consistent with previous literature. Moreover, the coverage of the secondary structures does not appear to affect the receding CAs when only the high-adhesion regime is considered. This can be explained by the contact line dynamics model proposed by Gao and McCarthy.[28,44] The authors argued that on a hierarchically structured surface, advancing of a liquid droplet is achieved by sections of the front liquid/vapor interface descending onto the next microblocks to be wet. Thus, the roughness of the tops of the microstructures does not greatly affect this process. On the other hand, in a receding event, the edge of the contact region must disjoin from entire post tops in concerted events, and the energy required for this process depends heavily on the details of the liquid/solid interfaces and the nanometer-scale features on the top of the microposts.

Furthermore, there did not seem to be a direct correlation between the average-dosage of the second exposure and the receding CA. In fact, in some cases the same normalized dosage gave two distinctive behaviors with receding CAs differing for as much as 43°. To understand the main factors that account for the large variation of surface adhesion among samples where the EBL parameters and fabrication protocol were only slightly different, a closer examination, atomic force microscopy (AFM) measurements, on the surface topology of the secondary structures was necessary. It should be mentioned that AFM measurements were only performed on the plateau of the primary features. Representative images of both high- and low-adhesion surfaces are presented in Figure 3. Our measurements indicate that a secondary-feature aspect ratio by itself does not directly correlate with CA hysteresis. It was found that low-hysteresis surfaces can be produced with either high- or low-aspect-ratio secondary structures. Among the low-adhesion surfaces, it is the one with a moderate aspect ratio that gives the highest receding CA (Figure 3a). By comparing the secondary-features of low-adhesion (Figure 3a) and high-adhesion (Figure 3b) surfaces, it can be concluded that the decisive factor that leads to low or high adhesion is the profile of the nanofeatures. For low adhesion surfaces, the tops of the secondary-structures are flat with sharp edges transitioning to their side walls. The high-adhesion surfaces all contained secondary nanofeatures with rounded or even pointed tops, as seen in Figure 3b. The flat tops and steep sidewalls of the low-adhesion nanofeatures contribute to contact-line pinning and therefore the stabilization of the Cassie state on the secondary structures. This, in turn, lowers the total contact area and increases the receding CA. The variation in surface properties under similar fabrication protocols highlights the sensitivity of the fabrication technique to small changes in resist thickness, substrate properties, and e-beam exposure parameters. Some work is still needed to increase the consistency and yield of low adhesion superhydrophobic surfaces beyond the level achieved here.

## 4. Conclusions

To conclude, we have introduced a novel, versatile, and efficient e-beam technique for fabricating macroscopic hierarchical superhydrophobic surfaces, which allows for precise control

over both the primary and the secondary structures. We have explained in detail how to manipulate the feature-spacing (from 200 nm to 500 nm), shape (either ridges or posts), and distribution (either over the entire surface or only on the tops of the primary structures) of the secondary-structures. Surfaces produced by this technique are used to quantitatively study the structure–property relations of superhydrophobicity. The main results are: First, we confirm that the advancing CA is insensitive to the spacing, shape, or distribution of the secondary-features. Second, we found that two distinct regimes can be reached by similar hierarchical structures, and that the determining factor is not the aspect-ratio but rather the sharpness of the transition from the top to the sidewall of the secondary structures. Third, the receding CA of low-adhesion surfaces does not exhibit clear dependency on the secondary-feature spacing. Fourth, the receding CA of high-adhesion surfaces increases by approximately 3° per 100 nm increase in secondary-feature spacing. Quite some work remains before a complete understanding of the physics behind wetting phenomena can be achieved. We believe that the technique developed here can serve as a useful tool with which the effect of hierarchical surface structures on wetting and adhesion can be studied systematically with unprecedented versatility and precision.

## 5. Experimental Section

*Materials and Equipment*: SU-8 2015 and SU-8 2000.5 resists were purchased from MicroChem. 3-inch reclaimed wafers (thickness: 525 ≈ 725 μm; type, orientation, and resistivity: any) were purchased from WRS Materials. Silicon monoxide pieces (99.9% pure) and a tungsten boat were purchased from Kurt J. Lesker. (Tridecafluoro-1,1,2,2-tetrahydrooctyl)-dimethylchlorosilane (>95%) were purchased from Gelest. JEOL JSM-7001F thermal field wmission SEM instrument with Nanometer Pattern Generation System (NPGS) were used for EBL. Edwars Auto 306 thermal evaporator were used for thermal deposition. STS Vision 320 Reactive Ion Etch system were used for plasma etching.

*Single-Exposure E-Beam Lithography*: SU-8 2015 was first spin-coated onto a 3 in. wafer via a three-step process: 1) The spin coating was started at 100 rpm $sec^{-1}$, accelerated to 500 rpm, and then continued at 500 rpm for 5 s; 2) The spin coating was started at 500 rpm $sec^{-1}$, accelerated to 2000 rpm, and then continued at 2000 rpm for 7 s; 3) The spin coating was started at 1000 rpm $sec^{-1}$, accelerated to 4000 rpm, and then continued at 4000 rpm for 28 s. After being soft baked at 95 °C for 5 min and slow cooling to room temperature, the wafer was carefully diced into 1 cm × 1 cm pieces. A two-dimensional 50 × 50 array (total area 1 mm × 1 mm) of 10 μm × 10 μm or 8 μm × 8 μm squares with a 20 μm period was generated in the DesignCAD Express. The center-to-center distance (CCD) and line spacing (LS) were both set to 500 nm in the NPGS. Parameters of the EBL were the following: 30 kV acceleration voltage, 6 mm working distance, 130× magnification, 80 ≈ 220 pA beam current (PC 6 ≈ 8), 0.05 ≈ 0.15 nC $cm^{-1}$ line dosage (a smaller dose produced thinner bridges between the blocks). The post exposure bake (PEB) of 5 min at 95 °C and the subsequent development in an SU-8 developer for 30 ≈ 60 seconds were carried out immediately after the NPGS. An optional final hardening bake at 100 °C for 15 min was also carried out for some of the samples. In casees of making the alternating structures, two CAD files were drawn, each corresponding to one type (either smooth or rough) of blocks, and the CCD and LS for the smooth ones were set to be 100 nm in the e-beam. All other conditions were identical to the ones above.

*Double-Exposure E-Beam Lithography*: The first exposure was done similar to a single-exposure e-Beam. The only changes were: The CAD design was a 100 × 100 array (covering a total area of 2 mm × 2 mm), the magnification was 60×, CCD and LS were both 100 nm, the PC was 10 ≈ 11 (600 ≈ 700 pA), the area dosage was 1.4 μC $cm^{-2}$, and the development was omitted. After the PEB of the first exposure, the sample was slowly cooled down to room temperature, then spin-coating was performed a second time on top of the first layer with a SU-8 2000.5 at 3500 rpm for 30 s. The CAD design for the second exposure was a 200 μm × 200 μm square and CCD and LS were both 200, 300, 400, or 500 nm. The small-scale e-beam lithography was completed with 10 × 10 writings (mechanical stage movement in between writings); the magnification of each writing was 650×, the beam current was 80 ≈ 250 pA, and the line dosage was 0.03 ≈ 0.15 nC $cm^{-1}$. Following the second exposure was another PEB at 95°C for 3 min and finally a 1 min development in PGMEA.

*Silanization*: A 6 nm layer of SiO was first deposited onto the SU-8 structures, then the surface underwent an oxygen plasma treatment for 60 s with the following settings: the power was 200 W, the pressure was 250 mTorr, and the $O_2$ flow rate was 50 sccm. The samples were immediately transferred into a closed reaction chamber, where the silanization was carried out at 80 °C for 4 d. The initial silane (liquid) volume ratio was 1% with respect to the chamber volume. After the silanization, all samples were washed with, in this order, acetone, IPA, and DI wafer, and finally dried with nitrogen.

*SEM Imaging*: A 10nm layer of gold was first deposited with a CHA SE-600 electron-beam evaporator, then the sample was scanned in a JEOL JSM-7001F Thermal FE-SEM at 5 kV acceleration voltage.

*AFM Scanning*: A Veeco Dimension 3100 atomic force microscope equipped with an RTESP probe was used to acquire AFM images. Tapping mode was used with scan rate of 1.0Hz, a driving amplitude of 1.05 ≈ 1.20V, an integral gain of 0.3, and a proportional gain of 0.5. Data was then analyzed with Gwyddion.[45]

*CA Measurements*: Digital images were aquired with an EO-1312C 1/2-inch CMOS Color USB camera and microscope lens from Edmund Optics. The images where then analyzed with ImageJ.[43] Data fitting was performed with Numpy[46] and plotting with a Python package Matplotlib.[47]

## Acknowledgements

The authors gratefully acknowledge support from the NSF Center for Hierarchical Manufacturing at UMASS (Grant number CMMI-0531171). We would also like to extend our appreciations to Stefan Dickert, Nicholas Hendricks, and John Nicholson for the helpful discussions.

Received: March 26, 2011
Published online: July 11, 2011

[1] K. Koch, B. Bhushan, W. Barthlott, *Prog. Mater. Sci.* **2009**, *54*, 137–178.
[2] B. Bhushan, Y. C. Jung, *Prog. Mater. Sci.* **2011**, *56*, 1–108.
[3] E. Munch, M. E. Launey, D. H. Alsem, E. Saiz, A. P. Tomsia, R. O. Ritchie, *Science* **2008**, *322*, 1516–1520.
[4] X. Feng, L. Jiang, *Adv. Mate.* **2006**, *18*, 3063–3078.
[5] W. Zhao, L. Wang, Q. Xue, *J. Phys. Chem. C* **2010**, *114*, 11509–11514.
[6] L. F. Boesel, C. Greiner, E. Arzt, A. del Campo, *Adv. Mater.* **2010**, *22*, 2125–2137.
[7] G. S. Watson, B. W. Cribb, J. A. Watson, *ACS Nano* **2010**, *4*, 129–136.
[8] L. Lin, M. Liu, L. Chen, P. Chen, J. Ma, D. Han, L. Jiang, *Adv. Mater.* **2010**, *22*, 4826–4830.
[9] X. Yao, Q. Chen, L. Xu, Q. Li, Y. Song, X. Gao, D. Quere, L. Jiang, *Adv. Funct. Mater.* **2010**, *20*, 656–662.
[10] K. Koch, B. Bhushan, Y. C. Jung, W. Barthlott, *Soft Matter* **2009**, *5*, 1386–1393.

[11] W. Barthlott, T. Schimmel, S. Wiersch, K. Koch, M. Brede, M. Barczewski, S. Walheim, A. Weis, A. Kaltenmaier, A. Leder, H. F. Bohn, *Adv. Mater.* **2010**, *22*, 2325–2328.
[12] C. Greiner, E. Arzt, A. del Campo, *Adv.d Mater.* **2009**, *21*, 479–482.
[13] J. Wu, J. Xia, Y. Zhang, W. Lei, B. Wang, *Physica E* **2010**, *42*, 1325–1328.
[14] F. Zhang, H. Y. Low, *Langmuir* **2007**, *23*, 7793–7798.
[15] B. Balu, V. Breedveld, D. W. Hess, *Langmuir* **2008**, *24*, 4785–4790.
[16] S. J. Choi, S. Y. Huh, *Macromol. Rapid Commun.* **2010**, *31*, 539–544.
[17] F. Sauvage, F. Di Fonzo, A. Li Bassi, C. S. Casari, V. Russo, G. Divitini, C. Ducati, C. E. Bottani, P. Comte, M. Graetzel, *Nano Lett.* **2010**, *10*, 2562–2567.
[18] H. Wu, D. Lin, W. Pan, *Langmuir* **2010**, *26*, 6865–6868.
[19] Y. Kwon, N. Patankar, J. Choi, J. Lee, *Langmuir* **2009**, *25*, 6129–6136.
[20] B. Bhushan, Y. C. Jung, K. Koch, *Philos. Trans. R. Soc. A* **2009**, *367*, 1631–1672.
[21] Y. Xiu, L. Zhu, D. W. Hess, C. P. Wong, *Langmuir* **2006**, *22*, 9676–9681.
[22] X. Yao, L. Xu, L. Jiang, *Adv. Funct. Mater.* **2010**, *20*, 3343–3349.
[23] H. Ko, Z. Zhang, K. Takei, A. Javey, *Nanotechnology* **2010**, *21*, 295305.
[24] A. H. F. Wu, K. L. Cho, I. I. Liaw, G. Moran, N. Kirby, R. N. Lamb, *Faraday Discuss.* **2010**, *146*, 223–232.
[25] Y. Xiu, Y. Liu, D. W. Hess, C. P. Wong, *Nanotechnology* **2010**, *21*, 155705.
[26] M. Nosonovsky, *Langmuir* **2007**, *23*, 3157–3161.
[27] J. Shieh, F. J. Hou, Y. C. Chen, H. M. Chen, S. P. Yang, C. C. Cheng, H. L. Chen, *Adv. Mater.* **2010**, *22*, 597–601.
[28] L. Gao, T. J. McCarthy, *Langmuir* **2006**, *22*, 2966–2967.
[29] Y. Xiu, S. Zhang, V. Yelundur, A. Rohatgi, D. W. Hess, C. P. Wong, *Langmuir* **2008**, *24*, 10421–10426.
[30] R. Xiao, K. H. Chu, E. N. Wang, *Appl. Phys. Lett.* **2009**, *94*, 193104.
[31] M. Byun, R. L. Laskowski, M. He, F. Qiu, M. Jeffries-EL, Z. Lin, *Soft Matter* **2009**, *5*, 1583–1586.
[32] W. Han, M. Byun, L. Zhao, J. Rzayev, Z. Lin, *J. Mater. Chem.* **2011**, DOI: 10.1039/C1JM10978B.
[33] H. Yang, P. Jiang, *J. Colloid and Interface Sci.* **2010**, *352*, 558–565.
[34] B. Pokroy, S. H. Kang, L. Mahadevan, J. Aizenberg, *Science* **2009**, *323*, 237–240.
[35] M. Morariu, N. E. Voicu, E. Schaffer, Z. Lin, T. P. Russell, U. Steiner, *Nat. Mater.* **2003**, *2*, 48–52.
[36] T. Baldacchini, J. E. Carey, M. Zhou, E. Mazur, *Langmuir* **2006**, *22*, 4917–4919
[37] H. Chen, E. Kern, C. Ziegler, A. Eychmuller, *J. Phys. Chem. C* **2009**, *113*, 19258–19262.
[38] Q. Xiao, T. Yang, A. Ursache, M. T. Tuominen, *J. Appl. Phys.* **2008**, *103*, 07C521
[39] B. Bilenberg, S. Jacobsen, M. S. Schmidt, L. H. D. Skjolding, P. Shi, P. Bogild, J. O. Tegenfeldt, A. Kristensen, *Microelectron. Eng.* **2006**, *83*, 1609–1612.
[40] M. Salerno, R. Cingolani, *J. Micromech. Microeng.* **2007**, *17*, 2414–2419.
[41] D. López-Romero, C. A. Barrios, M. Holgado, M. F. Laguna, R. Casquel, *Microelectron. Eng.* **2010**, *87*, 663–667.
[42] A. del Campo, C. Greiner, *J. Micromech. Microeng.* **2007**, *17*, R81–R95.
[43] ImageJ is an open source image processing program developed at the National Institutes of Health. More information about ImageJ can be found on: http://rsbweb.nih.gov/ij/(last accessed, June 2011).
[44] L. Gao, T. J. McCarthy, *Langmuir* **2006**, *22*, 6234–6237.
[45] Gwyddion is an open source software for SPM data visualization and analysis. More information about Gwyddion can be found on: http://gwyddion.net (last accessed, June 2011).
[46] Numpy is an open source extension to Python for numerical computations. More information about Numpy can be found on: http://numpy.scipy.org (last accessed, June 2011).
[47] Matplotlib is plotting library for Python. More information about Matplotlib can be found on: http://matplotlib.sourceforge.net (last accessed, June 2011).